Urban Climate 41 (2022) 101081

Contents lists available at ScienceDirect

Urban Climate

journal homepage: www.elsevier.com/locate/uclim

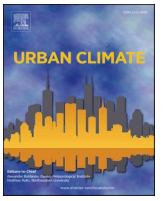

Overlapping heat and COVID-19 risk in New York City

L. Ortiz [a,*], A. Mustafa [a], P. Herreros Cantis [a], T. McPhearson [a,b,c]

[a] Urban Systems Lab, The New School, New York, NY, USA
[b] Cary Institute of Ecosystem Studies, Millbrook, NY, USA
[c] Stockholm Resilience Centre, Stockholm University, Stockholm, Sweden

ARTICLE INFO

Keywords:
Extreme heat
Multi-hazard risk
Covid-19
Vulnerability
New York City

ABSTRACT

New York City, the most populated urban center in the United States, is exposed to a variety of natural hazards. These range from extratropical storms and coastal flooding to extreme heat and cold temperatures, and have been shown to unevenly impact the various vulnerable groups in the city. As the COVID-19 pandemic hit in March 2020 and the city became an early epicenter, disparities in exposure led to widely uneven infection and mortality rates. This study maps the overlapping heat and COVID-19 risks in New York City with a multi-hazard risk framework during Summer 2020. To do so, we simulate neighborhood scale temperatures using the Weather Research and Forecasting model coupled with a multi-layer urban parameterization. Simulation outputs were combined with zipcode-scale COVID-19 and sociodemographic data to compute a multi-hazard risk index. Our results highlight several regions where high social vulnerability, COVID-19 infection rates, and heat coincide. Moreover, we use the local indicators of spatial association technique to map regions of spatially correlated high multi-hazard risk in the NYC boroughs of The Bronx and parts of Brooklyn and Queens. These high risk locations account for nearly a quarter of the city's population, with households earning less than half than those in the lowest risk zones.

1. Introduction

New York City (NYC) is the largest urban center in the US, with a population of over 8 million and a wider metropolitan area with over 20 million people. Historically, the city has been impacted by a variety of natural hazards that range from extratropical storms and coastal and fluvial flooding, to extreme heat and cold (González et al., 2019). These hazards result in impacts ranging from increased mortality and power outages due to extreme heat to disruption of public transportation due to flash flooding, among others. Heat stroke deaths average 13 per year in NYC, while increasing the probability of mortality for those with pre-existing comorbidities like heart disease and asthma (Madrigano et al., 2015). Extreme heat also stresses the electric grid, causing outages and brownouts. Examples include the recent extreme heat events in July 2019 and June 2021 causing power outages to over 5000 and 50,000 households, respectively (Anjileli et al., 2021; Sundstrom, 2021). These blackouts can in turn increase mortality rates. Research on the August 2003 citywide outage in NYC found that non-accidental death increased by 25%, while accidental deaths increased by 128%, resulting in at least 90 excess deaths. Global climate change is also expected to intensify these impacts, with heat related mortality projected to increase between 47 and 95% according to a study combining global climate projections and mortality records for NYC (Knowlton et al., 2007).

* Corresponding author.
E-mail address: ortizl@newschool.edu (L. Ortiz).

https://doi.org/10.1016/j.uclim.2021.101081
Received 4 October 2021; Received in revised form 19 December 2021; Accepted 30 December 2021
Available online 4 January 2022

Moreover, exposure to natural hazards may disproportionately impact vulnerable groups due to urban development patterns, uneven investment in adaptations and critical infrastructure, and historical racist housing and zoning policies such as redlining, a practice by which neighborhoods were classified by a federally backed institution (the Home Owners' Loan Corporation) regarding the security of mortgage investments depending on attributes that included racial composition, systematically giving the lowest grade ("D", labelled as "hazardous" and colored in red) to neighborhoods with a majority of black residents (Rothstein, 2017). Based on these maps, banks systematically denied loans and mortgages in redlined neighborhoods until the practice was banned in the 1960s, although the socioeconomic effects are still visible (Jones, 2017; Mitchell et al., 2018). Recent studies have quantified the impacts of these housing and development practices on exposure and vulnerability to heat. An analysis across 108 US urban areas of remotely sensed surface temperatures found that neighborhoods within formerly redlined communities were consistently warmer by 2.6 °C and by as much as 7 °C, mostly attributed to a lack of green space and more impervious surface coverage (Hoffman et al., 2020). These results are supported by surveys of urban tree cover across 37 urban areas by Locke et al. (2021) (Locke et al., 2021) which found that redlined areas have on average half as much tree canopy as non-redlined counterparts, with results consistent regardless of city size. In NYC, these practices have resulted in low income, African American communities being disproportionately exposed to extreme heat, as reported by Hamstead et al. (2018) and Herreros-Cantis and McPheason (2021) using a combination of satellite imagery, high resolution landscape data (i.e. land cover and building geometry), and US Census demographic data (Hamstead et al., 2018; Herreros-Cantis and McPhearson, 2021).

This increased exposure and lack of investment has resulted in disproportionate impacts to vulnerable communities. A study of social vulnerability found that in NYC, For example, the 2019 and 2020 heat waves disproportionately caused blackouts in lower income neighborhoods with large minority populations (Con Edison Media Relations, 2019). Meanwhile, in a study of all warm season deaths in NYC, Madrigano et al. (Madrigano et al., 2015) found that the odds of mortality during extreme heat increase more for non-hispanic black people and those living in rent-assisted housing compared to the rest of the population. These disparities persist across hazards. Households exposed to flooding associated with Hurricane Sandy were linked to higher social vulnerability, often belonging to lower income or older residents (Lieberman-Cribbin et al., 2020a).

1.1. COVID-19 in NYC

As the COVID-19 epidemic reached the US in early 2020, NYC became its first epicenter, leading the nation in case rates and mortality (Angel et al., 2020). Early research on nationwide patterns of which populations were more likely to be infected or have high mortality rates identified socioeconomic disparities across nearly all indicators (Dasgupta, 2020; Gaynor and Wilson, 2020; Wang et al., 2020a). Similar inequities were replicated within cities themselves, as identified early on for NYC by a body of research (Cordes and Castro, 2020; Fu and Zhai, 2021; Lieberman-Cribbin et al., 2020b; McPhearson et al., 2020) at neighborhood scales. These studies found that, in general, locations with a large share of low-income, black and persons of color populations correlated highly with COVID-19 positivity and mortality, as well as low amounts of testing.

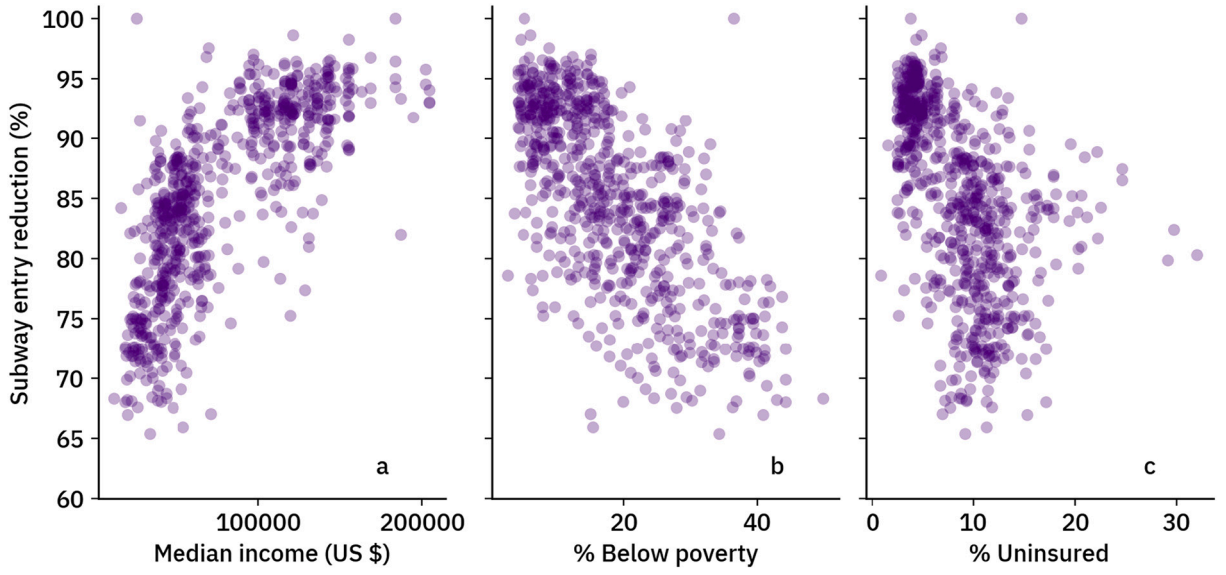

Fig. 1. Scatterplots of subway entry reduction and income-related socioeconomic indicators in NYC by station. Subway entry data was obtained from the MTA turnstile data portal (http://web.mta.info/developers/turnstile.html). The entry reduction was calculated by comparing the turnstile entries between two periods: a pre-pandemic interval (February 1st to February 7th 2020), and the first week after the State government declared a mandatory pause starting on March 22nd (March 21st to March 27th 2020). Income, poverty and insurance data was obtained from the American Community Survey (ACS) 5-year estimates at the Zip Code Tract Area, and spatially joined with the location of the subway stations.

These disparities in COVID-19 impacts have been attributed to higher unemployment rates and higher reliance on public transportation, as reported by Cordes and Castro (Cordes and Castro, 2020). These findings are consistent with subway use records by the New York Metropolitan Transportation Authority (MTA) during summer 2020. MTA records show that although there were massive reductions in subway usage across NYC due to statewide stay-at-home orders, there were significant disparities in the magnitude of that reduction. Across the city, subway stations in lower-income, high poverty level, and highly uninsured populations saw significantly lower reductions in total daily entries compared to days before stay-at-home orders, which may in part be due to a large share of so-called essential workers residing in those neighborhoods (Fig. 1).

1.2. Extreme heat in NYC

In cities, ambient temperatures are often higher than in surrounding rural areas, a phenomenon called the urban heat island (UHI). UHIs form as a result of significant modification of the land surface by changing natural landscapes to buildings, infrastructure, and impervious surfaces. These modifications can lead to significant reductions in natural cooling processes like evapotranspiration and radiative cooling, as well as additional heat generation (e.g., air conditioning) and storage in traditional building materials (Oke, 1982). In addition, studies have shown that these processes intensify during periods of extreme heat due to land-atmosphere feedback processes that lead to UHIs in the first place (Ao et al., 2019; Founda and Santamouris, 2017; Li and Bou-Zeid, 2013; Ortiz et al., 2018a; Ramamurthy et al., 2017), which include increased need for cooling, depletion of soil moisture, and increased stored heat.

The NYC UHI was first detailed via a field campaign by Bornstein (Bornstein, 1968), who reported a maximum urban-rural difference of 1.6 °C during the morning that decreased to zero at 310 m above the surface. Gedzelman et al. (Gedzelman et al., 2003) reported UHI intensity for NYC averaging 4 °C on summer nights. Further, they found that spatial features of the UHI varied significantly with time of day and prevailing meteorological conditions. For example, afternoon sea-breezes from the southeast coast of Long Island often pushed the core of the UHI west, while nighttime weak land breezes led to a UHI forming over Brooklyn and Queens boroughs. More recent work in NYC (Ortiz et al., 2018a) found similar geospatial temperature distributions to Gedzelman et al. during a heat wave, with UHI intensity increasing from 1 to 2 °C to >5 °C as the large-scale signal from a regional heat wave fed into local land surface processes.

The spatially uneven distribution of the NYC UHI has led to an uneven distribution of extreme heat impacts. These impacts are reflected in higher heat-related mortality and hospitalization rates in high socioeconomic vulnerability areas (Madrigano et al., 2015). A multi-year study of heat related mortality in NYC found that during heat waves, deaths were more likely among non-hispanic black individuals, as well as in census tracts with a high proportion of economically assisted households (Madrigano et al., 2015; Rosenthal et al., 2014). These populations often reside in areas where the daytime UHI is highest (e.g., west and north of NYC). Further, households in these neighborhoods also had the lowest adoption rates of air conditioning in the city (Ito et al., 2018), with the onset of heat-related deaths and hospitalizations occurring most often in indoors spaces.

1.3. Multi-hazard risk framework

A growing body of work seeks to address the complexities of overlapping hazards and vulnerabilities using the concept of multi-hazard risk. For example, Byers et al. (Byers et al., 2018) explored global climate-related hazards impacts on population and infrastructure using a set of multi-hazard risk scores across various shared socioeconomic pathways (SSPs). Similar work leveraged kilometer-scale data with US Census socioeconomic indicators to create a set of multi-hazard risk projections for the US (Binita et al., 2021). At the city scale, Depietri and McPhearson (Depietri et al., 2018) used fine scale data on extreme heat, inland (pluvial) flooding, and coastal flood hazards combined with census block scale socioeconomic vulnerability indicators to create a multi-hazard risk index for NYC. A similar effort was carried out for two Hong Kong districts by Johson et al., analyzing typhoons, landslides, and extreme heat hazards (Johnson et al., 2016). In these studies, risk, defined as the potential harm produced by a hazard, includes not only the intensity and spatial extent of a hazard, but also the exposure, susceptibility, and coping capacity of a system (e.g., population, electric grids, etc).

Given potential overlaps in vulnerability to COVID-19 and weather-related hazards like extreme heat, response planning must account for the combined risks to vulnerable populations. Adaptation frameworks that consider a single hazard may increase difficulties in dealing with others. For example, public cooling centers may be most efficient when they serve a large population, but also serve as an enclosed high-transmission environment if ventilation and distancing is not adequate. Similarly, not accounting for various populations' exposure and capacity to cope with various hazards may paint a lopsided view of actual impacts.

Rather than exploring causal relationships between COVID and heat risks in the context of social vulnerability, the key objective of this study is to explore spatial correlations between multi-hazard risk (extreme heat and COVID-19) and social vulnerability in New York City. To accomplish this, we employ the Localized Indicators of Spatial Association (LISA) approach which is widely used to analyze multivariate clusters between natural hazards and social vulnerability (Gaither et al., 2011; Ge et al., 2021; Houghton and Castillo-Salgado, 2020; Tate et al., 2021). We use LISA to map hot and cold spots of multi-hazard risk during the height of the first wave of the COVID-19 pandemic. We leverage state-of-the-art urbanized numerical weather prediction in combination with NYC Department of Health and US Census socioeconomic data to assess the spatial patterns of overlapping risk in NYC.

2. Methods

Our work aims to quantify overlaps in extreme heat and COVID-19 risks, employing a combination of state-of-the-art urban scale

climate modeling, spatially explicit COVID-19 case data, and socioeconomic vulnerability indicators combined under a multi-hazard risk framework. We also map spatially associated clusters of high and low multi-hazard risk, as detailed in the sections below.

2.1. Multi-hazard risk and vulnerability indicators

In order to map population risk related to both heat and COVID-19, we employ the multi-hazard risk index as formulated by DePietri and McPhearson (Depietri et al., 2018), which considers hazards and vulnerabilities of a population,

$$R = H^{*}V$$

Here, H and V are normalized multi-hazard index and vulnerability indexes computed unweighted sums,

$$H = \frac{1}{n}\sum_{i=1}^{n} \alpha_i h_i$$

where n is the total number of hazards considered and h_i and w_i are the ith normalized hazard values and its corresponding importance weighting. In this study, hazards are weighted equally, although use of expert-based can be used to derive appropriate weighting factors as shown by DePietri and McPhearson (Depietri et al., 2018). Here we limit the hazards studied to COVID-19 and heat. We use total positive cases per 100,000 people for each Zip Code Tabulation Area (ZCTA) as an indicator of the COVID-19 hazard, as reported by the New York City Department of Health and Mental Hygiene (NYC DoHMH) (Fig. 2). ZCTAs are geographical boundaries composed of US Census Blocks meant to correspond with postal zip codes and are the basic area unit that the NYC Department of Health and Mental Hygiene uses to report COVID-19 statistics. COVID-19 case data was accessed November 20, 2021 and covers cumulative data up to August 31, 2020. This period includes data from the first case peak, which informed subsequent summer adaptations (e.g., stay at home orders, cooling center deployment).

Similarly, the vulnerability index is computed as

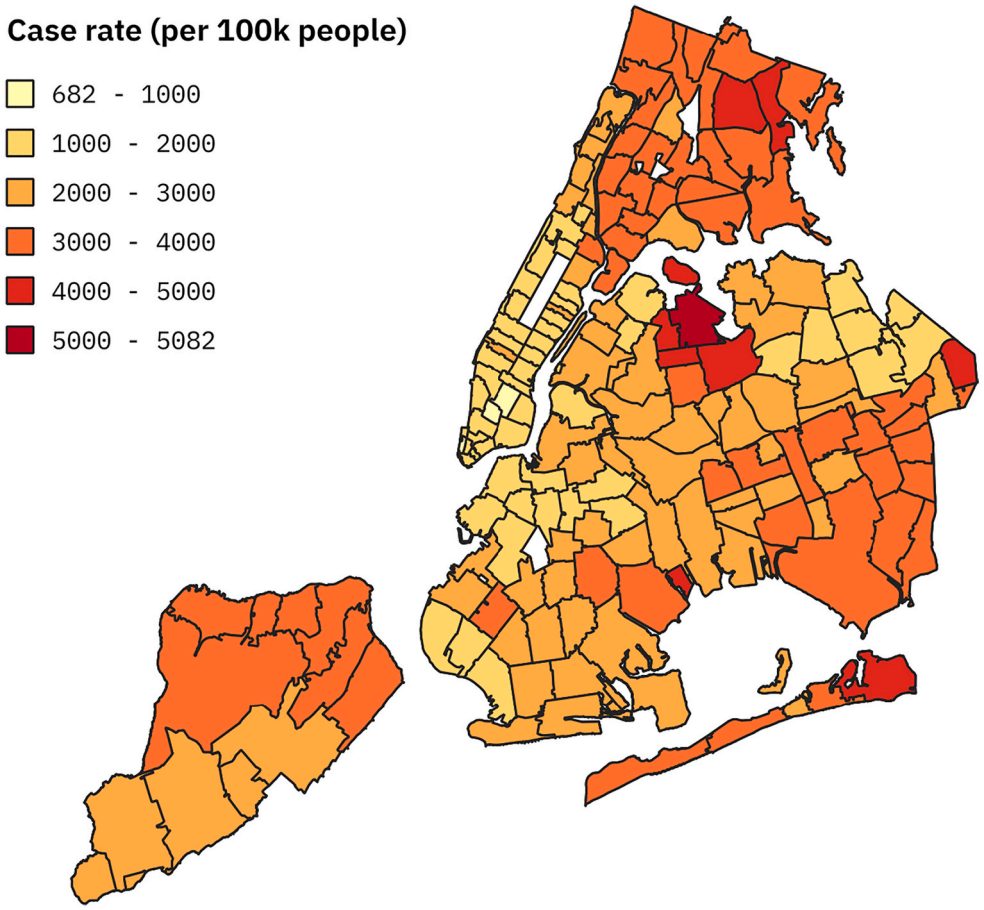

Fig. 2. Total positive COVID-19 tests per 100,000 residents (Accessed November 2021). Positive case rates in NYC were collected from hospitals and testing facilities by the NYC DoHMH and updated daily. Geometries without any assigned population or COVID-19 case data appear as white.

$$V = \frac{1}{k}\sum_{j=1}^{k} v_i$$

Here, each vulnerability indicator v_i is based on unweighted normalized socioeconomic vulnerability indicators calculated from the most recent update of the American Community Survey (ACS) 5-year estimates (2014–2018). The ACS indicators are a subset of those used in the US Centers for Disease Control (CDC) Social Vulnerability Index. An additional dataset, % population without health insurance, was also included as an indicator of access to healthcare in each. These vulnerability indicators correspond to exposure, lack of coping capacity, and susceptibility (Table 1).

Each indicator was aggregated to Zip Code Tabulation Areas (ZCTAs), which group all addresses with the same postal zip code under a common boundary. The indicators were tested for multicollinearity using a variance indicator factor (VIF) ≤ 5 as a threshold (Snee, 1973). The indicators were further reduced based on their relative importance as indicators of socioeconomic vulnerability based on McPhearson et al. (McPhearson et al., 2020), while maintaining indicators for exposure, lack of coping capacity, and susceptibility to the two hazards studied (Table x).

2.2. Urban climate model

We use the Weather Research and Forecasting model (WRF) (Skamarock et al., 2008) version 3.9 to simulate the summertime thermal environment in NYC. The urban canopy modifies the surface energy and momentum balance at the land surface by storing and generating heat, trapping and reflecting radiation, and inducing turbulence and drag to winds. To include the impact of these processes on the thermal environment, we use the multilayer Building Effect Parameterization (BEP) (Martilli et al., 2002) and Building Energy Model (BEM) (Salamanca et al., 2010) in combination with detailed urban canopy parameters (UCPs). WRF and the BEP-BEM sub-grid models have been used to model atmospheric processes in NYC including heat waves (Gutiérrez et al., 2015; Ortiz et al., 2018a), land-sea breeze interactions (Bauer, 2020), and multi-year demand for cooling (Ortiz et al., 2018b). The simulation period covers June 1 to August 31, 2020, with 5 days spinup time (May 27–31, 2020). Average daily maximum temperature for the summer period was used as a heat hazard indicator.

The parent domain used in the WRF simulations is centered around NYC and covers a significant portion of the Northeast US at a 9 km horizontal resolution, shown as the map extent in Fig. 3a. We use two nested subdomains with 3 km and 1 km horizontal resolution and two-way feedback option, so information from each subdomain is used by its parent domain in the subsequent calculation time step. The model was also configured with 51 vertical levels, with the 15 of them within the lowest 3 km of the atmosphere in order to resolve processes at the urban boundary layer. The highest resolution domain, D03 (Fig. 3a), contains the NYC Metropolitan area, which includes parts of New Jersey and Connecticut adjacent to the city. A time step of 54 s was used for the outer domain. Model sub-grid physics, tested in previous work in NYC (Gutiérrez et al., 2015; Ortiz et al., 2018a), are detailed in Table 2.

Urban geometry parameters, such as building heights, building area fraction, and building surface to plant area ratio were derived from the 2018 Primary Land-Use Tax Lot Output (PLUTO™) released by the NYC Department of City Planning (Fig. 3b-c) at a spatial resolution of 100 m. In addition, the land use classification used in PLUTO was aggregated into three urban classes (i.e., low and high density residential and commercial/industrial). In addition, UCPs that cannot be calculated from PLUTO, as well as data outside the NYC boundary was derived from the National Urban Data and Access Portal (NUDAPT) 1 km dataset, which covers areas outside NYC although at a coarser spatial resolution than PLUTO. Initial and boundary conditions were taken from the North American Regional Reanalysis (NARR) (Mesinger et al., 2006), which provides atmospheric and surface data fields at 32 km resolution for the contiguous United States.

The average of daily maximum temperatures was computed for the period between June 1 to August 31, as shown in Fig. 3f. In order to compare simulation outputs to COVID-10 cases and social vulnerability indicators, the 2-m air temperature field from the 1 km resolution D03 domain was aggregated to the NYC ZCTAs. The aggregation consisted of converting output fields (i.e., mean 2-meter daily maximum temperatures) into a point vector geometry layer, then using a spatial join with the ZCTA boundaries to associate each point to a ZCTA polygon. Where more than one WRF output coincided within a ZCTA, an average of all joined grid points was assigned.

2.3. Spatial correlation and hotspots analysis

In order to study spatial clustering of the combined heat and COVID-19 risk across ZCTAs, we employ LISA indicators (Anselin,

Table 1
Hazard and risk indicators used to compute the multi-hazard index.

	Indicator	Data source
Hazard	COVID-19	Total positive tests per 100,000 people
	Heat	Mean daily maximum 2-m temperature (Summer 2020)
Vulnerability	Exposure	Total population
	Lack of coping capacity	% Population > 65
		% Population w/o health insurance
		% Population below poverty
	Susceptibility	% Overcrowded households
		Median income (USD)
		% POC population

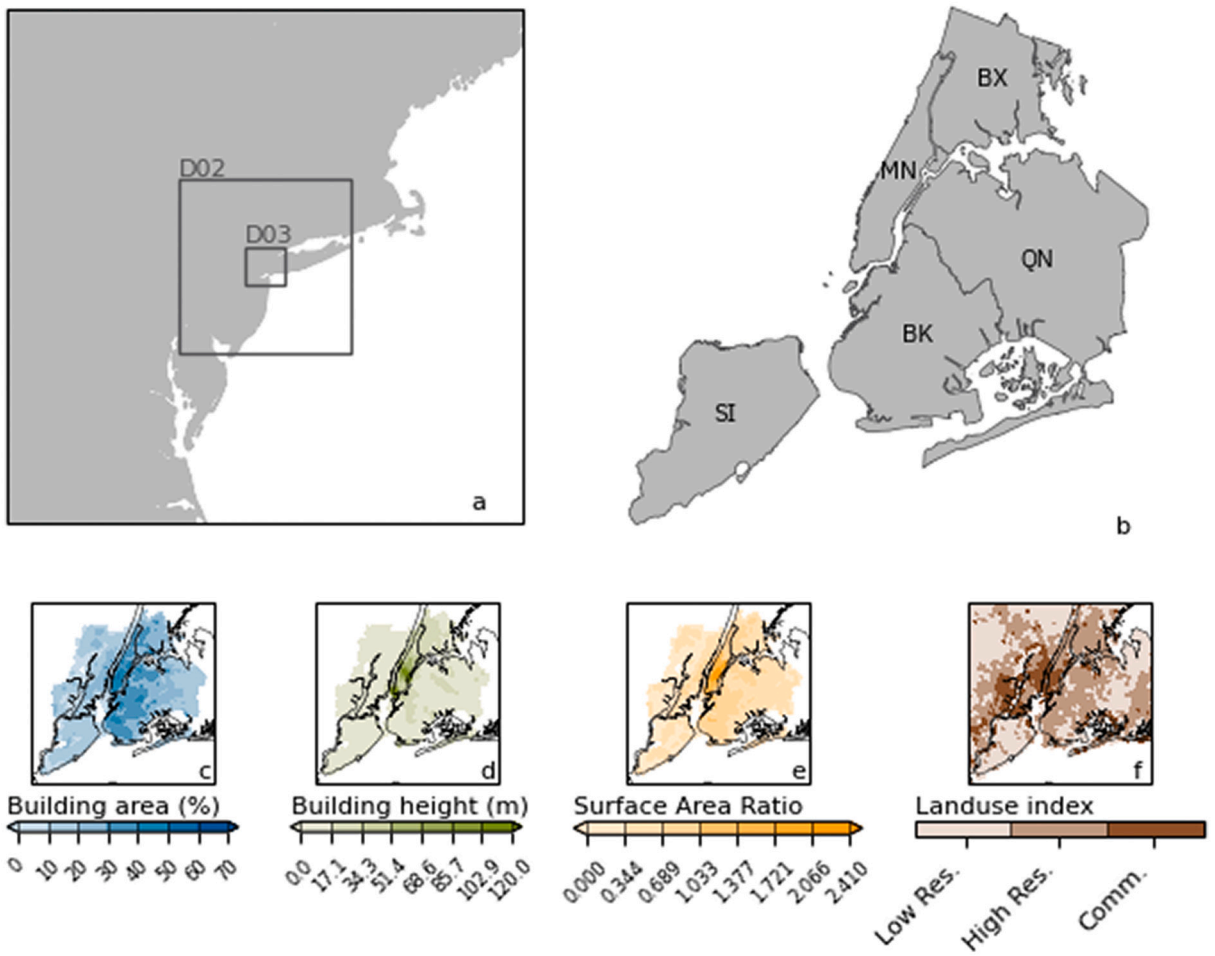

Fig. 3. (a) WRF simulation domain, with 9 km grid shown by figure extent, D02, and D03 marking the 3 km and 1 km sub-domains respectively. Panel (b) shows the five NYC boroughs of The Bronx (BX), Manhattan (MN), Brooklyn (BK), Queens (QN), and Staten Island (SI). Data derived from the PLUTO dataset include © building area fraction, (d) grid average building height, (e) grid average surface area to plant area ratio, and (f) urban land use index.

Table 2
WRF model physics sub-grid parameterization setup.

Model Physics	Selected parameterization
Land surface	NOAH LSM (Tewari et al., 2004)
Urban canopy	Building Effect Parameterization (Martilli et al., 2002) Building Energy Model (Salamanca et al., 2010)
Boundary layer	Mellor-Yamada-Janjic (Janjić, 1994)
Cumulus	Kain-Fritsch (Kain, 2004)
Microphysics	Thompson (Thompson et al., 2008)
Shortwave radiation	RRTMG (Iacono et al., 2008)
Longwave radiation	RRTM (Mlawer et al., 1997)

1995). Previous studies applied LISA approach to multidimensionally evaluate the existence of spatial clusters in social vulnerability and hazards. For instance, Gaither et al. (2011) employed LISA to explore the spatial clusters between wildland fire risk and social vulnerability in the Southeastern United States. Houghton and Castillo-Salgado (2020) used LISA to analyze the correlations between vulnerability to climate change and protective green building design strategies in two US cities (Austin, TX, and Chicago, IL). Tate et al. (2021) applied LISA to map hotspots where high flood exposure and high social vulnerability converge in the entire US. LISA computes the local Moran's I, a local spatial autocorrelation index to identify clusters of high and low values in the variable of interest, as well as the likelihood that the observed pattern is the result of purely random spatial allocation of values. We apply this process on the multi-hazard risk index detailed in Section 2.1 and map it to identify hot and cold spots. Hot spots are identified by contiguous high value

ZCTAs with high spatial correlations with neighboring features, while cold spots are identified by high correlation, low risk ZCTAs. To determine whether spatial correlations are statistically significant, the existing spatial distribution for each feature is compared against the case of completely randomly distributed values. This comparison is repeated by randomly assigned permutations to obtain a pseudo significance value that estimates the probability of the current spatial distribution occurring by random processes. Here, we used 999 permutations to compute the pseudo statistical significance value p.

3. Results

3.1. Urban climate model evaluation

Results from the WRF simulations were evaluated against data from the US National Oceanic and Atmospheric Administration (NOAA) Automated Surface Observing Systems (ASOS) weather stations located in NYC. Air temperature is measured at four locations located at Central Park (NYC), The Battery (JRB), John F. Kennedy Airport (JFK), and LaGuardia Airport (LGA), as shown in Fig. 4e. ASOS station data was resampled to an hourly time series and compared to simulation outputs from the closest WRF land grid (Fig. 4a–d). Mean absolute error ranged from 1.7 °C at JFK to 2.4 °C at LGA, with comparisons with JRB and NYC yielding values of 1.98 °C and 1.96 °C respectively.

Qualitatively, the spatial distribution of summer daily maximum temperatures (Fig. 4 f) are similar to those reported in the analysis from Gedzelman et al. (Gedzelman et al., 2003). Afternoon temperatures, as represented by daily maximum 2 m air temperatures increase with distance to the southeastern coast as a result of afternoon sea breeze which pushes the core of the NYC UHI to parts of The

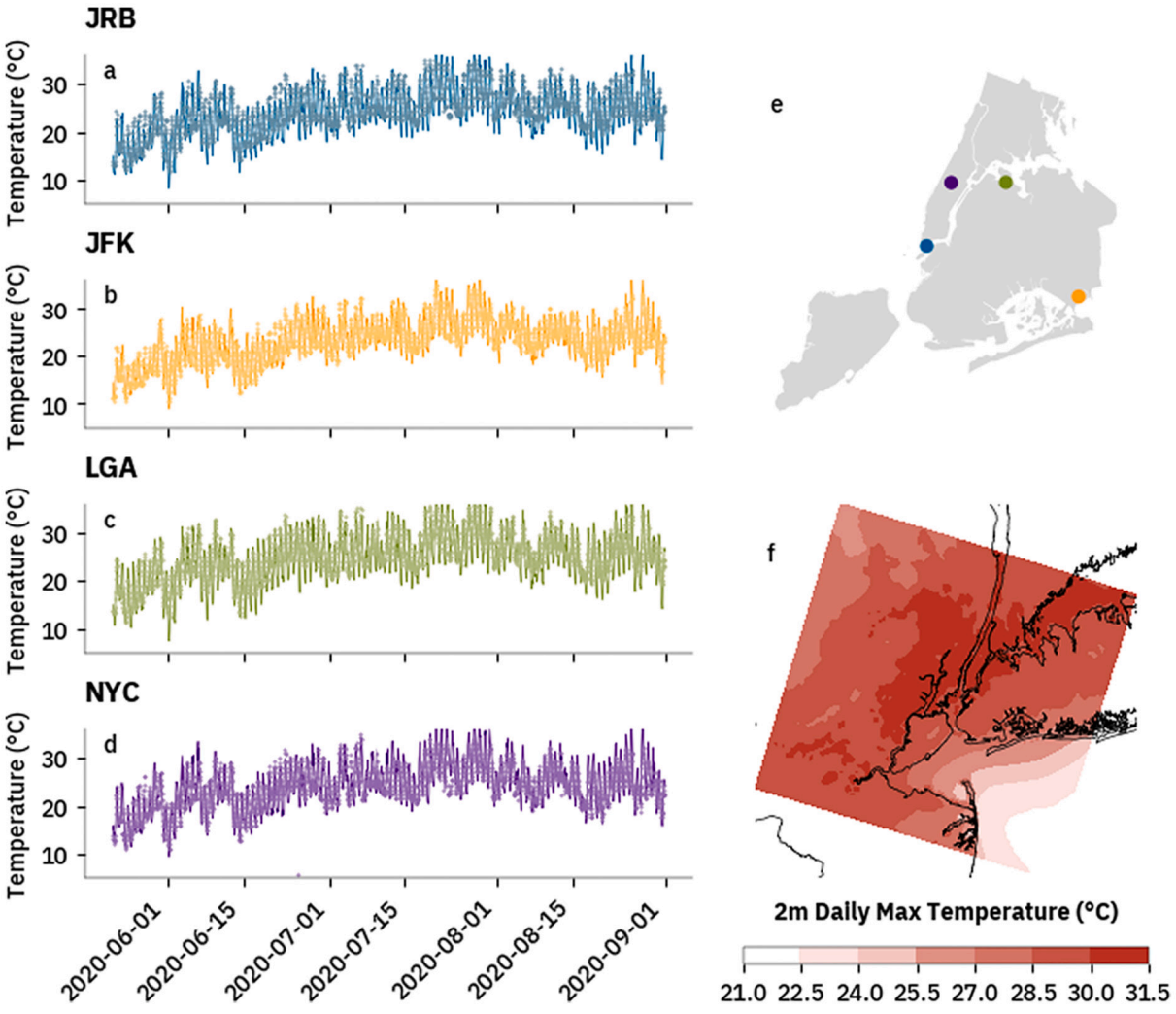

Fig. 4. Timeseries of air temperature at the ASOS stations and corresponding WRF simulation grid cell (a-d), station location (e), and average daily maximum temperatures for the simulation period (f). Station location marker colors (e) correspond to timeseries line and marker colors (a-d).

Bronx and New Jersey. Close to the southeast coast, mean afternoon temperatures are as low as 27.0 °C, while inland values reach close to 31 °C.

3.2. Vulnerability and risk

We map the computed vulnerability index (Fig. 5) by quartile, highlighting areas of low and high combined vulnerability. High vulnerability areas are located in historically low-income and minority-majority locations like The Bronx and significant portions of Brooklyn and Queens. Vulnerability is lowest in Manhattan, particularly around Central Park and below. However, areas of high vulnerability still exist in Manhattan and may even border low vulnerability areas such as East Harlem and the Upper East Side and the Lower East Side where Chinatown is located. This spatial distribution of social vulnerability was related to COVID-19 indicators (i.e., case rates, mortality, etc) by McPhearson et al. (McPhearson et al., 2020), who found significant overlaps between them throughout the first wave of the pandemic.

There are several overlaps between high vulnerability ZCTAs and the COVID-19 and heat hazards considered here. The largest of these overlaps covers a significant portion of The Bronx. There, afternoon temperatures are highest as the afternoon sea-breeze cools much of Brooklyn and Queens (Fig. 6, a) which moves the core of the daytime UHI north and west, and into parts of neighboring New Jersey (not pictured). Meanwhile, positivity rates during summer 2020 were also high throughout much of The Bronx, as detailed by Gedzelman et al. (Gedzelman et al., 2003). Another area with significant overlaps of high vulnerability and both hazards include the northern coast of Queens, in ZCTAs including the neighborhoods of Corona and Elmhurst. There are also regions where one hazard is high while the other is low. These include the entire southern coast of the city, where the aforementioned afternoon sea-breeze provides cooling, as well as midtown Manhattan, where high income populations for the most part were able to work from home or leave the city, reducing COVID-19 cases (Fig. 7, b).

Some of these patterns are observed when vulnerability, exposure, and both hazards are used to compute the multi-hazard risk index (Fig. 7). For example, most of The Bronx as well as ZCTAs in northern Queens rank in the top 25% of ZCTAS with high multi-hazard risk due to the overlaps of high vulnerability and both heat and COVID-19 hazard. Upper Manhattan is also a high multi-hazard risk area in spite of most of its ZCTAs ranking in the middle quartiles of COVID-19 risk. Meanwhile, the rest of Manhattan classifies into the middle quartiles due to the combination of high temperatures and low COVID-19 in spite of the lower vulnerability. Locations with overlapping low hazard and vulnerability also see a low risk score, such as most ZCTAs in the southern coast of Brooklyn and Queens.

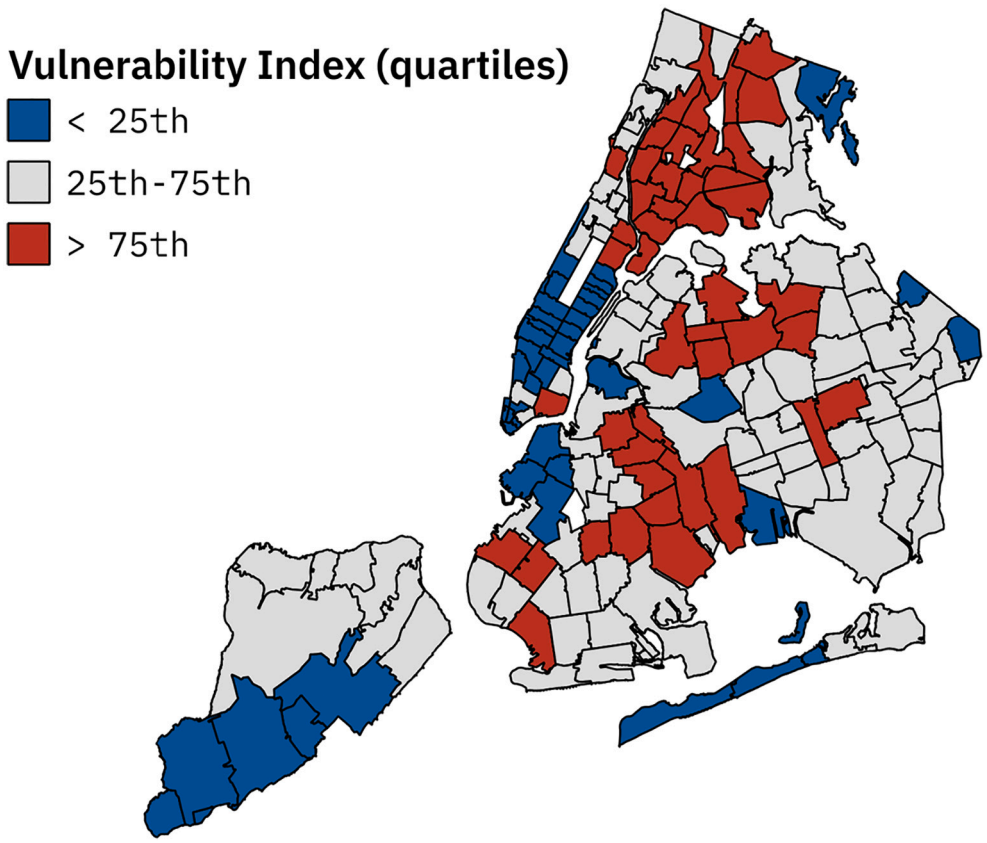

Fig. 5. Vulnerability index computed from the social vulnerability indicators for all NYC ZCTAs.

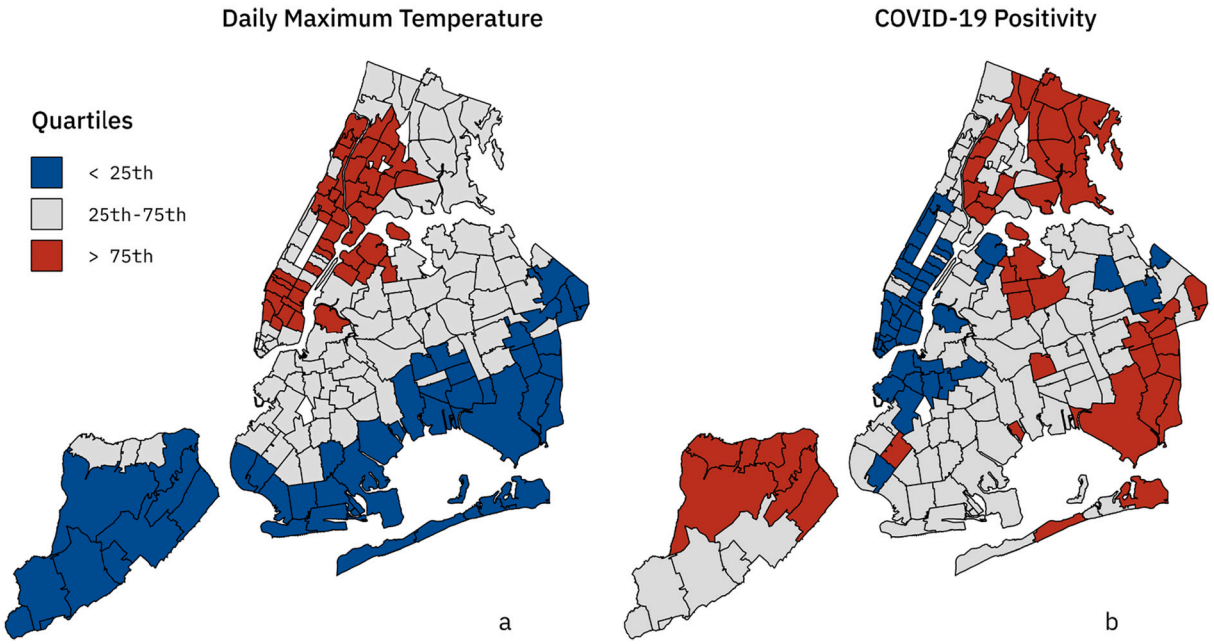

Fig. 6. Average daily maximum temperature and Summer 2020 COVID-19 positive cases per 100 k population at the time of the summer peak, divided into quartiles.

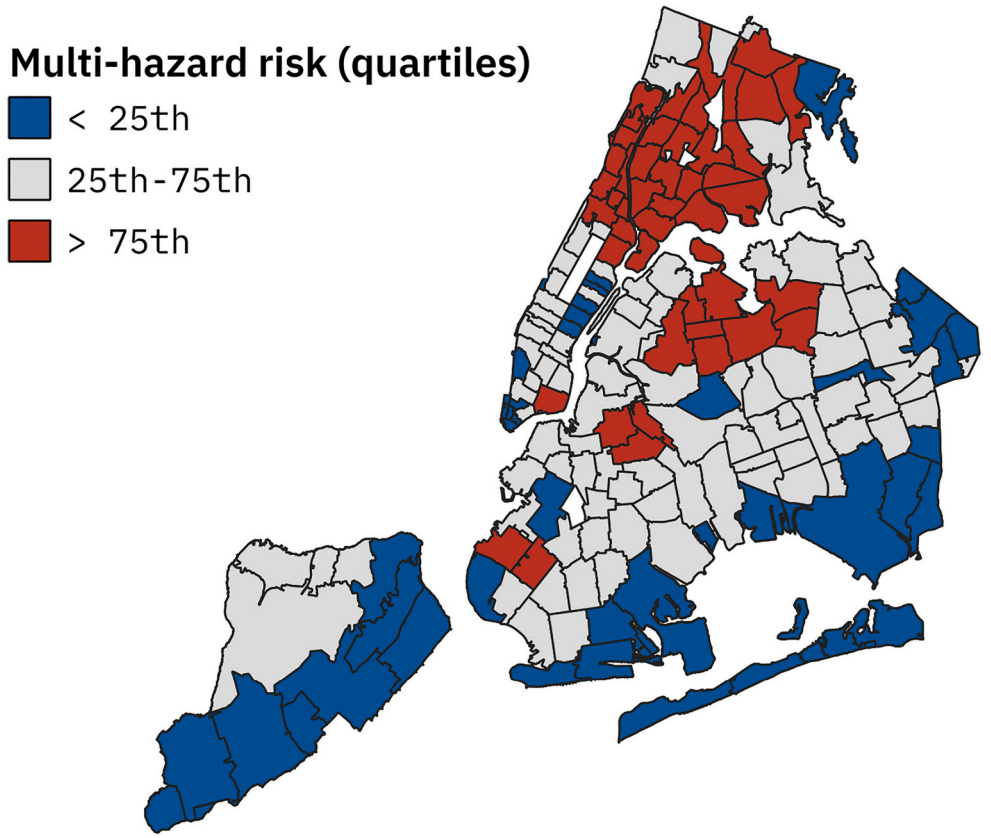

Fig. 7. Multi-hazard risk index for all NYC ZCTAs.

3.3. Multi-hazard risk spatial clustering

In order to study spatially associated clusters of high and low multi-hazard risk, we use the Local Indicators of Spatial Autocorrelation (LISA). Globally, the multi-hazard risk index has a Moran's I value of 0.753. This value is significantly higher than the expected Moran's I (−0.0057) for a completely random distribution of risk, indicating a high spatial autocorrelation at the city level. We compute the local Moran's I to quantify the spatial autocorrelation in risk within the city (Fig. 8, left). Results where high values of Moran's I are statistically significant at the $p < 0.05$ (Fig. 8, right) include the South Bronx, the southern tip of Manhattan, parts of Staten Island, north Queens, and Long Beach/Atlantic Beach to the south. In addition, there are ZCTAs with a weak spatial autocorrelation of multi-hazard risk, although none pass the statistical significance at the $p < 0.05$ level.

To group multi-hazard risk into high and low value spatial clusters, we plot the spatial lag of multi-hazard risk against the multi-hazard risk itself to obtain the Moran scatterplot (Fig. 9). The spatial lag for the value of a geometry is defined as the sum of that geometry's neighboring values, inversely weighted by distance. Here, values in the top right quadrant of the Moran scatterplot represent geometries where high risk values have a positive spatial autocorrelation while, values in the lower left quadrant show low values with high spatial autocorrelation. The data in these two quadrants represent hot (top right) and cold spots (bottom left). The data in the top left and bottom right quadrants represent geometries with high (or low) values surrounded by very low spatial autocorrelation.

Finally, we show the hot and cold spots of multi-hazard risk in NYC by segmenting the data using the LISAs as described above (Fig. 10) where the Moran's I value is statistically significant ($p < 0.05$). Results show two large hot spots, with the larger covering most of The Bronx and upper Manhattan, with another in the Queens neighborhoods of East Elmhurst and Corona. There are five cold spot clusters, with the largest (by total area) in Staten Island, with smaller clusters in lower Manhattan, the southern coast of Brooklyn, and the eastern edge of Queens. Although the Moran scatterplot (Fig. 9) showed ZCTAs with low spatial autocorrelations (i.e., high values among a group of low values, or low values among high values), none of these had a statistically significant relationship and are thus excluded.

4. Discussion and conclusions

In this study, we have created a multi-hazard risk index for COVID-19 and heat that accounts not only for the spatial distribution of the hazards but also population exposure and vulnerabilities. This study is the first city-wide exploration of the overlaps between one of the key pressing weather-related extremes (heat) and COVID-19. We leveraged NYC Department of Health reporting metrics with state-of-the-art urbanized climate models to quantify the spatial distribution of both hazards at fine spatial scales. In addition, we mapped spatially associated hot and cold spots of multi-hazard risk using local indicators of spatial association techniques. The hot spot analysis highlights uneven risks to the multi-hazard risk for large swaths of the NYC population. The hot spots include close to 2.04 million people (±7088), representing close to 23% of the city's population. Meanwhile cold spots house 573,000 (± 3684), accounting for around 6% of the city's total. Hot spots also tend to contain lower income households, with a median household income estimate of $41,638 per year, while households in cold spots earn $95,064 per year. The difference between the two groups for both median income and population are statistically significant ($p < 0.01$).

Our work can inform policymakers on the deployment of solutions to the overlapping heat and COVID-19 risks. For example, high multi-hazard risk areas may benefit most from programs offering free air conditioning units, reducing the need for communal cooling centers where virus transmission may happen more readily. Vaccine deployment may initially prioritize high multi-hazard risk neighborhoods in order to reduce transmission in cooling centers.

4.1. Limitations and future work

One limitation in our analysis is the lack of consideration of physiological risk factors to COVID-19 and extreme heat. Our current work only considers socioeconomic vulnerability indicators, rather than physiological ones. For example, respiratory and cardiovascular disease have been shown to influence COVID-19 severe illness and heat-related mortality (CDC, 2020; Lin et al., 2009; Soneja et al., 2016). These indicators may be used in future work, although there may be significant overlaps between high disease (i.e., cardiovascular or respiratory) and low income population in many cities (Cardet et al., 2018). Studies may also be expanded to account for non socioeconomic vulnerability indicators such as incidence of COVID-19 comorbidities (e.g., asthma, hypertension rates) that are not included here. Moreover, the consideration of adaptive capacity can be expanded by accounting for access to services like air conditioning (AC) access programs, parks and open spaces, and vaccination facilities. In addition, our analysis does not consider the magnitude of effect of the social vulnerability indicators studied on the impacts of hazard exposure to heat or COVID-19 (e.g., risk of severe illness), and rather describes where high vulnerability and hazard exposure coincide in space.

Future work can expand the multi-hazard risk index to include other independent hazards like coastal and inland flooding. Previous research in NYC has mapped overlaps in heat and these two flood types (Depietri et al., 2018), highlighting neighborhoods where all three combine with high vulnerability and exposure. Other hazards like high pollutant concentrations can also be considered, and may be a particularly useful indicator of both enhanced COVID-19 (Wang et al., 2020b) and heat-related mortality (McCormack et al., 2016; Wu et al., 2019). Future work can expand this framework to a comparative study across other cities with differences in size, density, weather hazards, and COVID-19 policies.

Another limitation in our work comes from the relatively coarse spatial resolution in our WRF simulations at 1 km. While this grid spacing is considered relatively high in numerical weather prediction, it may not capture intra-neighborhood or intra-ZCTA variations

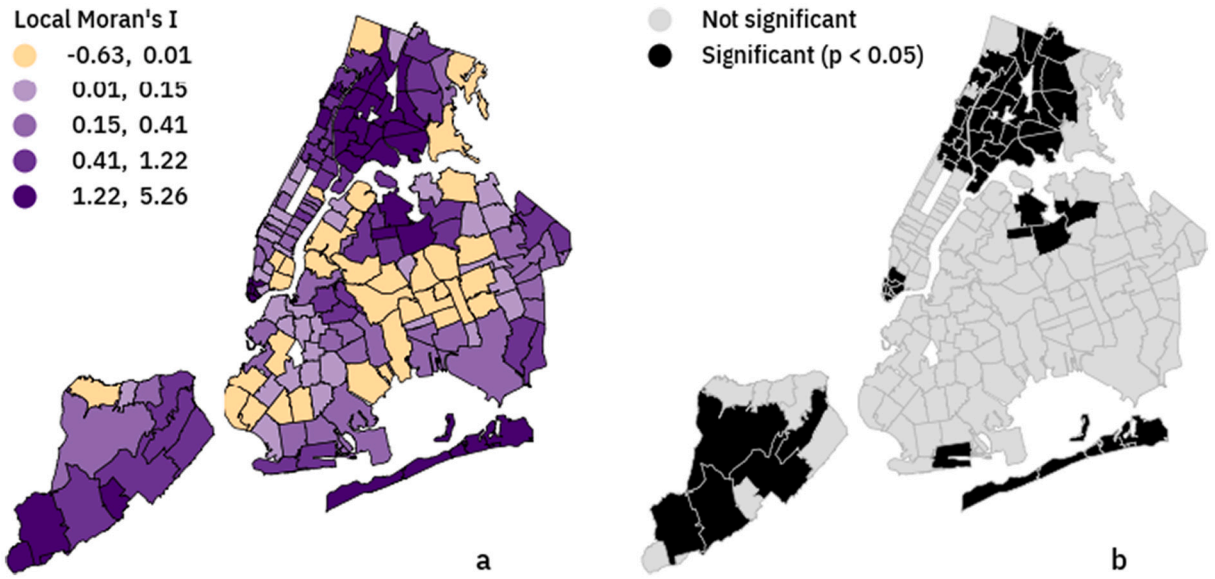

Fig. 8. Local Moran's I coefficients for each NYC ZCTA of the multi-hazard risk index (left) and each geometry's risk autocorrelation significance tested against the randomly allocated neighbors ($p < 0.05$).

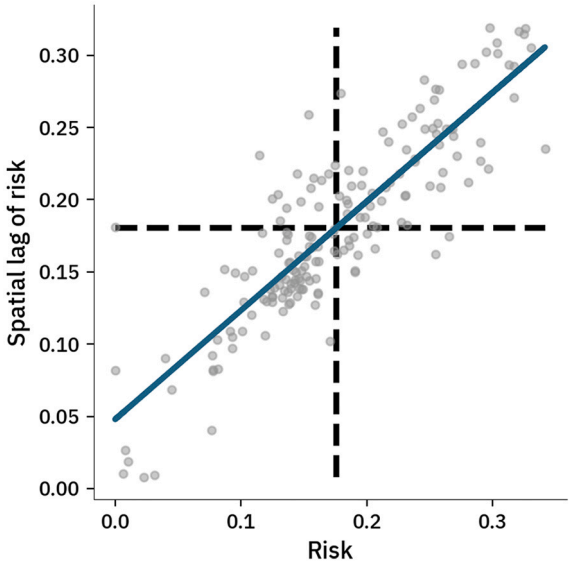

Fig. 9. Scatter plot of the spatial lag of the multi-hazard risk against the values of multi-hazard risk for each ZCTA. Dark blue line represents the linear fit between the two variables, while the black dashed lines are centered at the mean of risk and spatial lag of risk to form the Moran scatterplot. (For interpretation of the references to color in this figure legend, the reader is referred to the web version of this article.)

in near surface temperature that may occur due to differences in tree canopy cover, built environment materials, and street orientation. Future work may include the use of micro-meteorological models (Lindberg et al., 2018; McRae et al., 2020) to estimate these fine-scale features, although their computational cost often limits their use to short periods (e.g., ~1 day) and spatial extent (e.g., single neighborhood or city block).

Our analysis shows presented hereshows how disparities in the spatial extent and intensity of weather-related hazards can overlap with the ongoing COVID-19 pandemic. Previous work has demonstrated uneven impacts to NYC populations to both COVID-19 and heat individually. However, the highly transmissible nature of the COVID-19 virus complicates solutions to other hazards. The multi-hazard approach presented here maps the locations in NYC where these multi-hazard risks are particularly high that need solutions to each hazard that don't increase exposure to the other. This method may serve as a template to consider a variety of overlapping hazards to ensure a just response to not only the COVID-19 pandemic, but future similar outbreaks or weather-related perils.

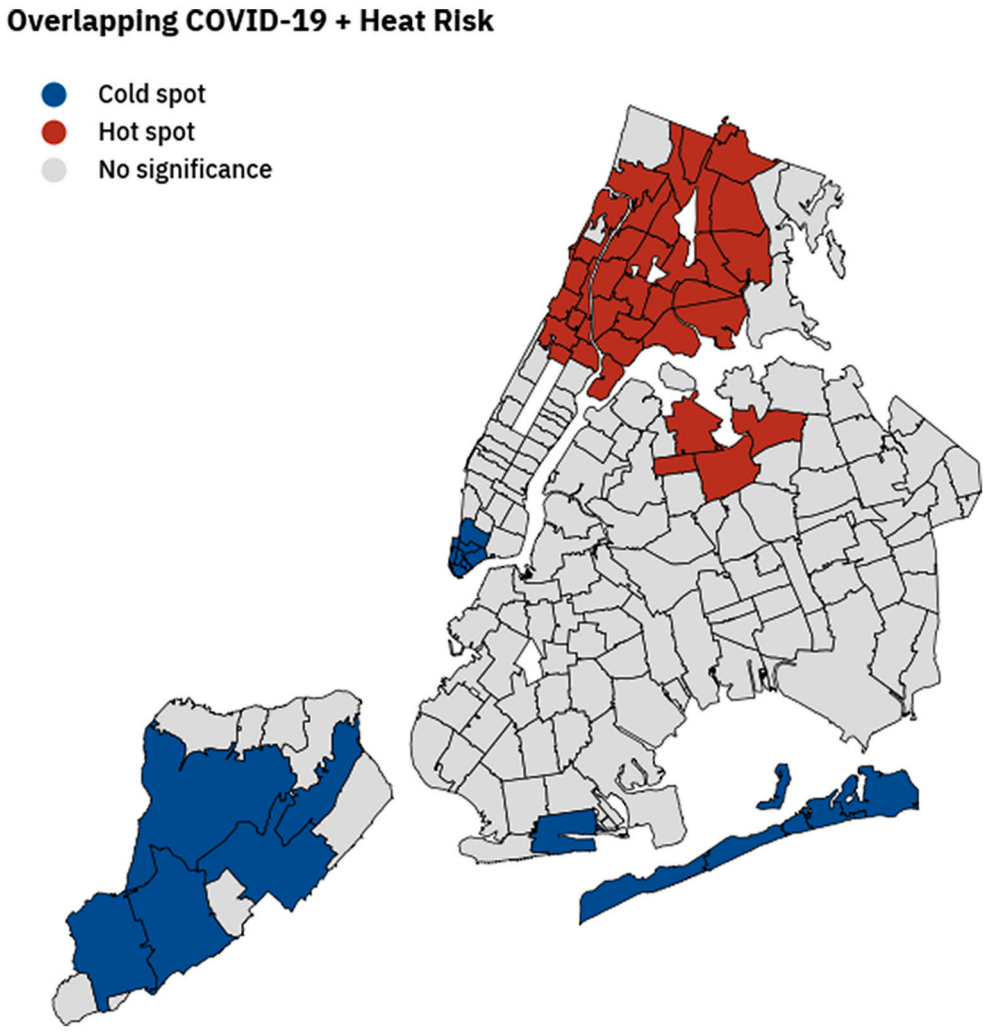

Fig. 10. Map of multi-hazard risk hot and cold spots in NYC. ZCTAs colored gray have no statistically significant ($p < 0.05$) spatial autocorrelation.

Declaration of Competing Interest

The authors declare that they have no known competing financial interests or personal relationships that could have appeared to influence the work reported in this paper.

Acknowledgments

This work was supported by the US National Science Foundation (Grants. #2029918 and #1934933). The authors also acknowledge the open source analytics libraries used in all analyses and figures, including pandas (Reback et al., 2021), geopandas (Jordahl et al., 2020), and Matplotlib (Hunter, 2007).

References

Angel, S., Blei, A.M., Lamson-Hall, P., Salazar Tamayo, M.M., 2020. The Coronavirus and the Cities: Explaining Variations in U.S. Metropolitan Areas as of 27 March 2020.
Anjileli, H., Huning, L.S., Moftakhari, H., Ashraf, S., Asanjan, A.A., Norouzi, H., AghaKouchak, A., 2021. Extreme heat events heighten soil respiration. Sci. Rep. 11 (1), 6632.
Anselin, L., 1995. Local indicators of spatial association—LISA. Geogr. Anal. 27 (2), 93–115.
Ao, X., Wang, L., Zhi, X., Gu, W., Yang, H., Li, D., 2019. Observed synergies between urban Heat Islands and heat waves and their controlling factors in Shanghai, China. J. Appl. Meteor. Climatol. 58 (9), 1955–1972.
Bauer, T.J., 2020. Interaction of Urban Heat Island Effects and Land–Sea Breezes during a New York City Heat Event. J. Appl. Meteorol. Climatol. 59 (3), 477–495.
Binita, K.C., Shepherd, J.M., King, A.W., Johnson Gaither, C., 2021. Multi-Hazard climate risk projections for the United States. Nat. Hazards 105 (2), 1963–1976.
Bornstein, R.D., 1968. Observations of the urban Heat Island effect in new York City. J. Appl. Meteorol. 7 (4), 575–582.

Byers, E., Gidden, M., Leclère, D., Balkovic, J., Burek, P., Ebi, K., Greve, P., Grey, D., Havlik, P., Hillers, A., Johnson, N., Kahil, T., Krey, V., Langan, S., Nakicenovic, N., Novak, R., Obersteiner, M., Pachauri, S., Palazzo, A., Parkinson, S., Rao, N.D., Rogelj, J., Satoh, Y., Wada, Y., Willaarts, B., Riahi, K., 2018. Global exposure and vulnerability to multi-sector development and climate change hotspots. Environ. Res. Lett. 13 (5), 055012.

Cardet, J.C., Louisias, M., King, T.S., Castro, M., Codispoti, C.D., Dunn, R., Engle, L., Giles, B.L., Holguin, F., Lima, J.J., Long, D., Lugogo, N., Nyenhuis, S., Ortega, V. E., Ramratnam, S., Wechsler, M.E., Israel, E., Phipatanakul, W., 2018. Income is an independent risk factor for worse asthma outcomes. J. Allergy Clin. Immunol. 141 (2), 754–760.e3.

CDC, 2020. COVID-19 and Your Health. Centers for Disease Control and Prevention [Online]. Available: https://www.cdc.gov/coronavirus/2019-ncov/need-extra-precautions/people-with-medical-conditions.html (Accessed: 19-Dec-2021).

Con Edison Media Relations, 2019. Con Edison Working To Restore Power To Approximately 33,000 Customer Outages In Some Southeast Brooklyn Neighborhoods [Online]. Available: https://www.coned.com/en/about-us/media-center/news/20190721/con-edison-working-to-restore-power-to-33000-outages-in-southeast-brooklyn-neighborhoods (Accessed: 20-Sep-2021).

Cordes, J., Castro, M.C., 2020. Spatial analysis of COVID-19 clusters and contextual factors in new York City. Spatial and Spatio-temporal Epidemiology 34, 100355.

Dasgupta, S., 2020. Association between social vulnerability and a County's risk for becoming a COVID-19 hotspot — United States, June 1–July 25, 2020. MMWR Morb. Mortal. Wkly Rep. 69.

Depietri, Y., Dahal, K., McPhearson, T., 2018. Multi-Hazard risks in new York City. Nat. Hazards Earth Syst. Sci. 18 (12), 3363–3381.

Founda, D., Santamouris, M., 2017. Synergies between urban Heat Island and heat waves in Athens (Greece), during an extremely hot summer (2012). Sci. Rep. 7 (1).

Fu, X., Zhai, W., 2021. Examining the spatial and temporal relationship between social vulnerability and stay-at-home behaviors in new York City during the COVID-19 pandemic. Sustain. Cities Soc. 67, 102757.

Gaither, C.J., Poudyal, N.C., Goodrick, S., Bowker, J.M., Malone, S., Gan, J., 2011. Wildland fire risk and social vulnerability in the southeastern United States: an exploratory spatial data analysis approach. Forest Policy Econ. 13 (1), 24–36.

Gaynor, T.S., Wilson, M.E., 2020. Social vulnerability and equity: the disproportionate impact of COVID-19. Public Adm. Rev. 80 (5), 832–838.

Ge, Y., Dou, W., Wang, X., Chen, Y., Zhang, Z., 2021. Identifying Urban–Rural Differences in Social Vulnerability to Natural Hazards: A Case Study of China. Nat. Hazards 108 (3), 2629–2651.

Gedzelman, S.D., Austin, S., Cermak, R., Stefano, N., Partridge, S., Quesenberry, S., Robinson, D.A., 2003. Mesoscale aspects of the urban Heat Island around new York City. Theor. Appl. Climatol. 75 (1–2), 29–42.

González, J.E., Ortiz, L., Smith, B.K., Devineni, N., Colle, B., Booth, J.F., Ravindranath, A., Rivera, L., Horton, R., Towey, K., Kushnir, Y., Manley, D., Bader, D., Rosenzweig, C., 2019. New York city panel on climate change 2019 report chapter 2: new methods for assessing extreme temperatures, heavy downpours, and drought. Ann. N. Y. Acad. Sci. 1439 (1), 30–70.

Gutiérrez, E., González, J.E., Martilli, A., Bornstein, R., Arend, M., 2015. Simulations of a heat-wave event in new York City using a multilayer urban parameterization. J. Appl. Meteorol. Climatol. 54 (2), 283–301.

Hamstead, Z.A., Farmer, C., McPhearson, T., 2018. Landscape-based extreme heat vulnerability assessment. J. of Extr. Even. 05 (04), 1850018.

Herreros-Cantis, P., McPhearson, T., 2021. Mapping supply of and demand for ecosystem services to assess environmental justice in new York City. Ecol. Appl. 31 (6), e02390.

Hoffman, J.S., Shandas, V., Pendleton, N., 2020. The effects of historical housing policies on resident exposure to intra-urban heat: A study of 108 US urban areas. Climate 8 (1), 12.

Houghton, A., Castillo-Salgado, C., 2020. Analysis of correlations between neighborhood-level vulnerability to climate change and protective green building design strategies: A spatial and ecological analysis. Build. Environ. 168, 106523.

Hunter, J.D., 2007. Matplotlib: A 2D graphics environment. Computing in science & engineering 9 (03), 90–95.

Iacono, M.J., Delamere, J.S., Mlawer, E.J., Shephard, M.W., Clough, S.A., Collins, W.D., 2008. Radiative forcing by Long-lived greenhouse gases: calculations with the AER radiative transfer models. J. Geophys. Res. 113 (D13), D13103.

Ito, K., Lane, K., Olson, C., 2018. Equitable access to air conditioning: A City health Department's perspective on preventing heat-related deaths. Epidemiology 29 (6), 749–752.

Janjić, Z.I., 1994. The Step-Mountain eta coordinate model: further developments of the convection, viscous sublayer, and turbulence closure schemes. Mon. Weather Rev. 122 (5), 927–945.

Johnson, K., Depietri, Y., Breil, M., 2016. Multi-Hazard risk assessment of two Hong Kong districts. International Journal of Disaster Risk Reduction 19, 311–323.

Jones, J., 2017. The racial wealth gap: how African-Americans have been shortchanged out of the materials to build wealth. Economic Policy Institute 13.

Jordahl, K., Bossche, J.V.D., Fleischmann, M., Wasserman, J., McBride, J., Gerard, J., Tratner, J., Perry, M., Badaracco, A.G., Farmer, C., Hjelle, G.A., Snow, A.D., Cochran, M., Gillies, S., Culbertson, L., Bartos, M., Eubank, N., Maxalbert Bilogur, A., Rey, S., Ren, C., Arribas-Bel, D., Wasser, L., Wolf, L.J., Journois, M., Wilson, J., Greenhall, A., Holdgraf, C., Leblanc, F., 2020. Geopandas/Geopandas: V0.8.1, Zenodo.

Kain, J.S., 2004. The Kain–Fritsch Convective Parameterization: An Update. J. Appl. Meteorol. 43 (1), 170–181.

Knowlton, K., Lynn, B., Goldberg, R.A., Rosenzweig, C., Hogrefe, C., Rosenthal, J.K., Kinney, P.L., 2007. Projecting heat-related mortality impacts under a changing climate in the new York City region. Am. J. Public Health 97 (11), 2028–2034.

Li, D., Bou-Zeid, E., 2013. Synergistic interactions between urban Heat Islands and heat waves: the impact in cities is larger than the sum of its parts. J. Appl. Meteorol. Climatol. 52 (9), 2051–2064.

Lieberman-Cribbin, W., Gillezeau, C., Schwartz, R.M., Taioli, E., 2020a. Unequal social vulnerability to hurricane sandy flood exposure. J Expo Sci Environ Epidemiol 1–6.

Lieberman-Cribbin, W., Tuminello, S., Flores, R.M., Taioli, E., 2020b. Disparities in COVID-19 testing and positivity in new York City. Am. J. Prev. Med. 59 (3), 326–332.

Lin, S., Luo, M., Walker, R.J., Liu, X., Hwang, S.-A., Chinery, R., 2009. Extreme high temperatures and hospital admissions for respiratory and cardiovascular diseases. Epidemiology 20 (5), 738–746.

Lindberg, F., Grimmond, C.S.B., Gabey, A., Huang, B., Kent, C.W., Sun, T., Theeuwes, N.E., Järvi, L., Ward, H.C., Capel-Timms, I., Chang, Y., Jonsson, P., Krave, N., Liu, D., Meyer, D., Olofson, K.F.G., Tan, J., Wästberg, D., Xue, L., Zhang, Z., 2018. Urban multi-scale environmental predictor (UMEP): an integrated tool for City-based climate services. Environ. Model Softw. 99, 70–87.

Locke, D.H., Hall, B., Grove, J.M., Pickett, S.T.A., Ogden, L.A., Aoki, C., Boone, C.G., O'Neil-Dunne, J.P.M., 2021. Residential housing segregation and urban tree canopy in 37 US cities. npj Urban Sustain 1 (1), 1–9.

Madrigano, J., Ito, K., Johnson, S., Kinney, P.L., Matte, T., 2015. A case-only study of vulnerability to heat wave–RelatedMortality in new York City (2000−2011). Environ. Health Perspect. 123 (7), 672–678.

Martilli, A., Clappier, A., Rotach, M.W., 2002. An urban surface exchange parameterisation for mesoscale models. Bound.-Layer Meteorol. 104 (2), 261–304.

McCormack, M.C., Belli, A.J., Waugh, D., Matsui, E.C., Peng, R.D., Williams, D.L., Paulin, L., Saha, A., Aloe, C.M., Diette, G.B., Breysse, P.N., Hansel, N.N., 2016. Respiratory effects of indoor heat and the interaction with air pollution in chronic obstructive pulmonary disease. Annals ATS 13 (12), 2125–2131.

McPhearson, T., Grabowski, Z.R., Herreros-Cantis, P., Mustafa, A., Ortiz, L., Kennedy, C., Tomateo, C., Lopez, B., Olivotto, V., Vantu, A., 2020. Pandemic Injustice: Spatial and Social Distributions of the First Wave of COVID-19 in the US Epicenter.

McRae, I., Freedman, F.R., Rivera, A., Li, X., Dou, J., Cruz, I., Ren, C., Dronova, I., Fraker, H., Bornstein, R., 2020. Integration of the WUDAPT, WRF, and ENVI-met models to simulate extreme daytime temperature mitigation strategies in San Jose, California. Build. Environ. 184, 1–18.

Mesinger, F., DiMego, G., Kalnay, E., Mitchell, K., Shafran, P.C., Ebisuzaki, W., Jović, D., Woollen, J., Rogers, E., Berbery, E.H., Ek, M.B., Fan, Y., Grumbine, R., Higgins, W., Li, H., Lin, Y., Manikin, G., Parrish, D., Shi, W., 2006. North American regional reanalysis. Bull. Am. Meteorol. Soc. 87 (3), 343–360.

Mitchell, B., Franco, J., Richardson, J., 2018. HOLC 'Redlining' Maps: The Persistent Structure of Segregation and Economic Inequality.

Mlawer, E.J., Taubman, S.J., Brown, P.D., Iacono, M.J., Clough, S.A., 1997. Radiative transfer for inhomogeneous atmospheres: RRTM, a validated correlated-k model for the longwave. J. Geophys. Res. 102 (D14), 16663.

Oke, T.R., 1982. The energetic basis of the urban Heat Island. Q. J. R. Meteorol. Soc. 108 (455), 1–24.
Ortiz, L.E., Gonzalez, J.E., Wu, W., Schoonen, M., Tongue, J., Bornstein, R., 2018a. New York City impacts on a regional heat wave. J. Appl. Meteorol. Climatol. 57 (4), 837–851.
Ortiz, L., González, J.E., Lin, W., 2018b. Climate change impacts on peak building cooling energy demand in a coastal megacity. Environ. Res. Lett. 13 (9), 094008.
Ramamurthy, P., González, J., Ortiz, L., Arend, M., Moshary, F., 2017. Impact of heatwave on a megacity: an observational analysis of new York City during July 2016. Environ. Res. Lett. 12 (5), 054011.
Reback, J., Jbrockmendel McKinney, W., Van Den Bossche, J., Augspurger, T., Cloud, P., Hawkins, S., Gfyoung, Sinhrks, Roeschke, M., Klein, A., Petersen, Terji, Tratner, J., She, C., Ayd, W., Hoefler, P., Naveh, S., Garcia, M., Schendel, J., Hayden, A., Saxton, D., Shadrach, R., Gorelli, M.E., Li, Fangchen, Jancauskas, V., McMaster, A., Battiston, P., Seabold, Skipper, Dong, Kaiqi, 2021. Pandas-Dev/Pandas: Pandas 1.3.2, Zenodo.
Rosenthal, J., Kinney, P.L., Metzger, K.B., 2014. Intra-urban vulnerability to heat-related mortality in new York City, 1997–2006. Health & Place 30, 45–60.
Rothstein, R., 2017. The Color of Law: A Forgotten History of how our Government Segregated America. Liveright Publishing Corporation, New York.
Salamanca, F., Krpo, A., Martilli, A., Clappier, A., 2010. A new building energy model coupled with an urban canopy parameterization for urban climate simulations—part I. formulation, verification, and sensitivity analysis of the model. Theor. Appl. Climatol. 99 (3–4), 331–344.
Skamarock, W., Klemp, J., Dudhia, J., Gill, D., Barker, D., Wang, W., Huang, X., Duda, M., 2008. A Description of the Advanced Research WRF Version 3.
Snee, R.D., 1973. Some aspects of nonorthogonal data analysis. J. Qual. Technol. 5 (2), 67–79.
Soneja, S., Jiang, C., Fisher, J., Upperman, C.R., Mitchell, C., Sapkota, A., 2016. Exposure to extreme heat and precipitation events associated with increased risk of hospitalization for asthma in Maryland, U.S.A. Environ. Health 15 (1), 57.
Sundstrom, M., 2021. Thousands without power across NY, NJ amid heat wave. PIX11.
Tate, E., Rahman, M.A., Emrich, C.T., Sampson, C.C., 2021. Flood exposure and social vulnerability in the United States. Nat. Hazards 106 (1), 435–457.
Tewari, M., Chen, F., Wang, W., Dudhia, J., LeMone, M., Mitchell, K., Ek, M., Gayno, G., Wegiel, J., Cuenca, R., 2004. "Implementation and Verification of the Unified NOAH Land Surface Model in the WRF Model," Seattle, WA, pp. 11–15.
Thompson, G., Field, P.R., Rasmussen, R.M., Hall, W.D., 2008. Explicit forecasts of winter precipitation using an improved bulk microphysics scheme. Part II: implementation of a new Snow parameterization. Mon. Wea. Rev. 136 (12), 5095–5115.
Wang, C., Li, Z., Mathews, M.C., Praharaj, S., Karna, B., Solís, P., 2020a. The spatial Association of Social Vulnerability with COVID-19 prevalence in the contiguous United States. Int. J. Environ. Health Res. 0 (0), 1–8.
Wang, B., Li, R., Lu, Z., Huang, Y., 2020b. Does comorbidity increase the risk of patients with COVID-19: evidence from Meta-analysis. Aging (Albany NY) 12 (7), 6049–6057.
Wu, Y., Zhao, K., Huang, J., Arend, M., Gross, B., Moshary, F., 2019. Observation of heat wave effects on the urban air quality and PBL in new York City area. Atmos. Environ. 218, 117024.